Measured and Predicted Pressure Distributions on the AFTI/F-111 Mission Adaptive Wing

Lannie D. Webb, William E. McCain, and Lucinda A. Rose

November 1988

NASA

National Aeronautics and
Space Administration

Measured and Predicted Pressure Distributions on the AFTI/F-111 Mission Adaptive Wing

Lannie D. Webb
Ames Research Center, Dryden Flight Research Facility, Edwards, California

William E. McCain and Lucinda A. Rose
PRC Systems Services, Edwards, California

1988

MEASURED AND PREDICTED PRESSURE DISTRIBUTIONS ON THE AFTI/F-111 MISSION ADAPTIVE WING

Lannie D. Webb
NASA Ames Research Center
Dryden Flight Research Facility
Edwards, California

William E. McCain and Lucinda A. Rose
PRC Systems Services
Edwards, California

Abstract

Flight tests have been conducted using an F-111 aircraft that has been modified with a mission adaptive wing (MAW). The MAW has variable-camber leading and trailing edge surfaces that can change the wing camber in flight, while preserving smooth upper surface contours. This paper contains wing surface pressure measurements obtained during flight tests at Dryden Flight Research Facility of NASA Ames Research Center. Upper and lower surface steady pressure distributions were measured along four streamwise rows of static pressure orifices on the right wing for a leading-edge sweep angle of 26°. The airplane, wing, instrumentation, and test conditions are discussed. Steady pressure results are presented for selected wing camber deflections flown at subsonic Mach numbers up to 0.90 and an angle-of-attack range of 5° to 12°. The Reynolds number was 26 million, based on the mean aerodynamic chord. The MAW flight data are compared to MAW wind-tunnel data, transonic aircraft technology (TACT) flight data, and predicted pressure distributions. The results provide a unique database for a smooth, variable-camber, advanced supercritical wing.

Nomenclature

Reference values in brackets, [ ], based on a trapezoidal planform at $\Lambda_{LE} = 26°$.

AFCS	automatic flight control system
AFTI	advanced fighter technology integration
AR	aspect ratio, b^2/S [5.14]
b	wing span, ft [56.55 ft]
CFD	computational fluid dynamics
c	streamwise local chord, ft
c_{av}	mean geometric chord, S/b [11.0 ft]
C_L	lift coefficient for airplane
c_{MAC}	mean aerodynamic chord, $2/S \int_0^{b/2} c^2 \, dy$ [11.2 ft]
c_n	section normal-force coefficient, $\int_0^1 \Delta C_p dx/c$
C_p	pressure coefficient, $(p - p_\infty)/q_\infty$
$C_{p_{L.S.}}$	pressure coefficient on wing lower surface
$C_{p_{U.S.}}$	pressure coefficient on wing upper surface
C_p^*	critical pressure coefficient, $[0.7547(1 + 0.2 M_\infty^2)^{3.5} - 1.4386]/M_\infty^2$
ΔC_p	lifting-surface pressure coefficient, $C_{p_{L.S.}} - C_{p_{U.S.}}$
DFRF	NASA Ames Dryden Flight Research Facility
MAW	mission adaptive wing
M_∞	free-stream Mach number
PCM	pulse code modulation
p	local static pressure, lb/ft^2
p_∞	free-stream static pressure, lb/ft^2
q_∞	free-stream dynamic pressure, lb/ft^2
R_e	Reynolds number, $\rho_\infty V_\infty c_{MAC}/\mu_\infty$
R_n	unit Reynolds number, ft^{-1}
S	wing reference area, ft^2 [622.0 ft^2]
TAA	transonic airfoil analysis

TACT	transonic aircraft technology
t	maximum local chord thickness, ft
V_∞	free-stream velocity, ft/sec
x	streamwise coordinate, ft
x/c	fraction of local streamwise chord
y	spanwise coordinate, ft
α	wing-reference angle of attack, deg
β	aircraft angle of sideslip, deg
$\delta_{LE/TE}$	leading/trailing edge camber deflection, deg
η	fraction of semispan, $2y/b$
λ	taper ratio, tip-to-root chord, c_t/c_r [0.635]
Λ_{LE}	leading-edge sweepback angle, deg
μ_∞	free-stream coefficient of viscosity, lb·sec/ft^2
ρ_∞	free-stream density, lb·sec^2/ft^4

Introduction

The wing for a tactical fighter airplane is typically designed for a few optimum or near-optimum flight conditions, such as 1-g cruise. However, the airplane has to operate over a wide range of flight conditions, which usually results in less-than-optimum overall performance at off-design conditions. The original design of the F-111 with a variable-sweep wing increased the number of optimum flight conditions. The transonic aircraft technology (TACT) program (Refs. 1,2) combined a supercritical airfoil (Ref. 3) with planform and twist changes to improve transonic cruise and maneuver performance relative to the conventional F-111 wing. The cruise design point of the TACT wing was for maximum range capability at Mach 0.85 (C_L = 0.45). Although significant improvements were made in the cruise and maneuver performance of the F-111 TACT, overall performance at off-design conditions could also be improved.

A wing configuration that would allow smooth camber changes throughout the flight envelope could provide optimum aerodynamic performance at all flight conditions. The design studies to develop a smooth, variable-camber, advanced supercritical wing resulted in the mission adaptive wing (MAW). This is part of a joint NASA/USAF/Boeing flight research program at Dryden Flight Research Facility (DFRF), NASA Ames Research Center to study advanced fighter technology integration (AFTI) (Ref. 4). The wing design process evolved through a series of iterations involving extensive wind-tunnel tests (Refs. 5,6), supplemented by theoretical analyses (Ref. 7). Consideration of such contraints as the structural design and implementation of the variable camber and flight control systems were included in this design process. The primary physical constraint imposed on the variable-camber wing design was a cost-saving measure that required the new wing to be built around the existing TACT wing box structure. The MAW cruise (undeflected camber) wing was designed for the same 1-g TACT cruise condition to provide a reference standard. The original TACT supercritical airfoil was replaced with an advanced, creepless, transonic airfoil to provide further performance improvements. The aerodynamic efficiency of the airfoil shape is further maintained at all camber settings due to the smooth upper surface contour provided by the unique internal mechanisms and flexible skin panels of the MAW. The MAW also has an automatic flight control system (AFCS) with four separate control modes that are currently being flight-tested. Reference 8 describes the function of each AFCS mode, and flight test results for one of the AFCS modes have been documented in Ref. 9.

Improving the F-111 TACT performance envelope was the primary design goal of the AFTI/F-111 MAW program. One objective of the AFTI/F-111 flight test program is to evaluate the MAW performance improvements relative to a conventional fixed-camber or hinged-flap wing. The technical database developed from this evaluation can be used to help transition the demonstrated technology to future military and civilian aircraft. Recent results from the MAW flight program have been published in Refs. 4, 9, 10, 11 and 12. The purpose of this paper is to present representative results from the MAW database. Measured surface pressure distributions and section normal-force coefficients will be discussed and compared to corresponding MAW wind-tunnel data, TACT flight data, and predicted data.

Description of Experiment

Airplane

The AFTI/F-111 airplane shown in Fig. 1 was initially an F-111A airplane that was modified for the F-111 TACT test aircraft. The TACT wing, except for the wing box, was replaced with the MAW system after the TACT program was completed. The AFTI/F-111 airplane is a modified two-place (side-by-side) fighter/bomber. Two Pratt and Whitney TF-30-P-9 axial flow, dual compressor turbofan engines, equipped with full modulating afterburners, provide

the thrust. The MAW system consists of an automatic flight control system (AFCS) combined with variable wing sweep and variable camber. Small modifications were made to the TACT planform and airfoil to accomodate installation of the smooth skin leading- and trailing-edge variable-camber system. The variable-camber leading and trailing edge surfaces of the MAW are illustrated in Fig. 2.

Wing

The wing development process, as referenced in the introduction (Refs. 7,10), evolved through a series of design iterations that began with the TACT wing. The primary physical constraint imposed on the variable-camber wing design was that the new wing be built around the existing TACT wing box structure. This limited all airfoil shape changes to the leading- and trailing-edge regions fore and aft of the wing box. An unconstrained wing design (relaxation of the wing box external contours) was investigated during the predesign study, but the baseline configuration for further development in the final design phase was a constrained design. Until the final design phase, the cruise wing geometries of the wind-tunnel models had been developed around the TACT wing box contours from the jig-shape wing. However, for the final design phase a camber and twist distribution representative of the 1-g cruise design shape was desired for a 1/12-scale wind-tunnel model (Ref. 13). This baseline configuration, designated wing model W2.4E, was used to obtain most of the wind-tunnel data. Due to the extensive data available, both in terms of geometric description and surface pressure measurements, the geometry for wing model W2.4E was used in the current computational model at NASA Ames DFRF. The TACT 1-g cruise wing (designated wing model W54) was also tested on the 1/12-scale model to allow direct comparisons between the F-111 TACT and AFTI/F-111 wings.

During the final design stage of the variable-camber flap mechanism, the wing was thickened in the outboard leading- and trailing-edge regions to accommodate the flap actuators. Because the original TACT wing inboard fixed trailing-edge segment was retained, the corresponding inboard end of the variable-camber trailing-edge flap had to be matched at this interface. The thickness of the trailing-edge flap at the inboard end was increased, and the recontour was faired out across the length of the flap using linear spanlines. The result was a slight modification to both the upper- and lower-surface contours of the variable-camber trailing-edge inboard flap segment. A final modification to

the wing involved opening up small gaps between the variable-camber trailing-edge flap segments to prevent interference when the flaps are deflected. The wing incorporating all of the above changes was designated W2.6J for the jig-shape geometry and W2.6E for the 1-g cruise shape. The full-scale wing fabrication was made from W2.6J contours.

This paper will limit its discussion to the final full-scale MAW (W2.6E), the 1/12-scale MAW wind-tunnel model (W2.4E), and the TACT 1-g cruise wing (W54). Figure 3 presents a comparison of selected geometric characteristics of these three wing models at leading edge sweepback angle, $\Lambda_{LE} = 26°$. The W2.4E wing planform, as shown in Fig. 3, was extended at the tip to form a trapezoidal area planform. The full-scale geometric characteristics derived for this model are used as reference values within this paper. This reference trapezoidal area planform at $\Lambda_{LE} = 26°$ was also used to develop a three-dimensional computational fluid dynamics (CFD) wing model. These characteristic values include wing span b, area S, and taper ratio λ ($b = 56.66$ ft, $S = 622.0$ ft^2 and $\lambda = 0.635$). Four airfoil contours of the W2.4E model that correspond to the surface pressure measurement locations are also shown in Fig. 3.

Instrumentation

The layout of the static pressure instrumentation for the right wing of the AFTI/F-111 MAW airplane is shown in Fig. 4. There are 152 flush static pressure orifices located on the upper and lower surfaces in four chordwise rows aligned with the freestream airflow at $\Lambda_{LE} = 26°$. Pressure orifices were installed into the smooth skin of the leading- and trailing-edge variable-camber system, while thirty were added to the existing orifices on the upper surface of the original TACT wing box (Ref. 14) at $\eta = 0.59$ and 0.76. The total number of upper and lower orifices at each semispan station are also listed on Fig. 4. The data presented in the following sections will not include measurements at every orifice location, due to anomulous conditions that were encountered from flight to flight. Nine of ten pressure transducer boxes are located inside the flexible leading- and trailing-edge flap surfaces of the MAW. Movement of the boxes required connecting the orifices in the leading- and trailing-edge surfaces with a flexible fluoro-silicon tubing of 0.07 in. internal diameter. The orifices located on the surface of the wing box are connected by stainless steel tubing of 0.12 in. internal diameter. The length of the pressure lines from the orifices to the transducers was limited to less

3

than 5 ft, thus minimizing pressure lag effects. Differential pressure transducers mounted in the 10 boxes were used to measure the differential pressure between the wing surface orifices and the reference pressure. A temperature-controlled, variable-capacitance, absolute pressure transducer (labeled reference transducer in Fig. 4) was used to measure the reference pressure. The pressure and performance parameters were recorded digitally on an airborne pulse code modulation (PCM) system. The PCM system has a sampling rate of 20 to 200 samples/sec (sps) with pressures sampled at 20 sps. A second digital PCM system on the aircraft was used to monitor the MAW instrumentation for control systems, loads, and flutter data.

Free-stream flight parameters ($M_\infty, p_\infty, q_\infty, \alpha$, and β) were measured and derived from sensors installed on the AFTI/F-111 air-data boom. Mach number data from a modified MA-1-type uncompensated pitot-static probe (Ref. 15) were corrected for position error. Angle of attack and sideslip were measured using a flight path accelerometer vane system (Ref. 16). The flow directions were corrected for boom bending, pitching moment, and upwash (Ref. 11) effects.

Test Conditions

Flight data are presented for subsonic Mach numbers up to 0.90 and an angle-of-attack range from 5° to 12°. Most of the flight data were obtained for a free-stream dynamic pressure of 300 lb/ft^2, a sideslip angle of 0°, and a unit Reynolds number of 2.3 × 10^6 ft^{-1} (26 × 10^6, based on $c_{MAC} = 11.2$ ft). Slow windup turns were flown to prescribed Mach number, angle of attack, and altitude conditions. At the desired, or target, flight condition for pressure measurements, the aircraft was stabilized in a sustained angle-of-attack turn for a short time period. In order to maintain α and M_∞, altitude was traded off. Flight conditions at $\alpha = 8°$ and 12° were of particular interest because there was a significant set of wind-tunnel data available for comparison. When selecting data for analysis, maximum deviations from the desired flight condition for M_∞ and α were 0.01 and 0.25°, respectively. Based on the repeatability of the airspeed calibration points, the accuracy of the measured M_∞ is estimated to be the same as that for the TACT program, ±0.005 (Ref. 1). Measurements of α and β have an estimated accuracy of ±0.25° (Ref. 1).

The flight maneuvers can be broken into two general categories: (1) steady state and (2) quasi-steady state. Most of the steady-state data were taken follow-

ing slow windup turns up to $\alpha = 8°$ or less while the airplane was stabilized in a sustained angle-of-attack turn. The airplane was difficult to stabilize for $\alpha > 8°$. Therefore, for most combinations of Mach number, wing camber deflection, and dynamic pressure, only quasi-steady-state data could be obtained for $\alpha > 8°$. In Fig. 5 the time history data for a particular flight illustrate both steady-state and quasi-steady-state maneuvers. The time history data includes the oscillatory acceleration of the normal acceleration at the wing tip, angle of attack, altitude, q_∞, and M_∞. The target flight conditions q_∞ and M_∞ were 300 lb/ft^2 and 0.85, respectively. The data plotted between 30 and 100 sec on the time scale were for a steady-state $\alpha = 8°$, with altitude traded off to maintain the other flight conditions. Between 100 and 120 sec, the pilot increased α to obtain the next test point at $\alpha = 12°$. During this time, the altitude loss increased rapidly while acceptable limits of M_∞ and q_∞ were exceeded. The pilot then attempted to reach $\alpha = 12°$, and once at the desired α, hold the other flight conditions steady. The short segment of data between 210 and 220 sec did maintain acceptable limits of α, M_∞ and q_∞, however, note that the wingtip-normal accelerometer indicates levels of wing buffet comparable to the 100–140 sec time segment. At both of these time segments near the $\alpha = 12°$ flight condition the maneuver is considered quasi-steady state and the data of marginal quality.

Flight Test Results

The following section presents selected MAW flight test data in the form of chordwise distributions of pressure coefficients C_p and section normal-force coefficients c_n. The influence of span effects, Mach number effects, angle-of-attack effects, and camber effects on the data is discussed. Certain expected features (Refs. 3, 17, 18, 19) in the flow field about supercritical wings such as the MAW are also discussed.

Span Effects

Figures 6(a) and (b) show steady chordwise C_p distributions at the four semispan stations for two Mach numbers, with $\delta_{LE/TE} = 0/2$ and α near 8°. Wind-tunnel data from the NASA Ames 11T tunnel (Ref. 5) are also plotted. The C_p distributions indicate attached flow over all four semispan stations in Fig. 6. At $M_\infty = 0.60$ a very large negative pressure peak (leading-edge suction) exists across the wing semispan for $\eta = 0.40, 0.59$, and 0.76, as shown in Fig. 6(a). This is a very significant flow feature, and the strength of the leading-edge suction can be referenced to the critical

4

pressure coefficient C_p^* level also shown in Figs. 6(a) and (b). Flight and wind-tunnel data show good agreement in most cases for $M_\infty = 0.60$. In Fig. 6(b) the flattop profile, typical of upper surface C_p distributions on supercritical airfoils (Ref. 3), has developed at all four semispan locations for $M_\infty = 0.85$. This supercritical-type pressure profile was expected for the camber deflection of $\delta_{LE/TE} = 0/2$ at the transonic cruise Mach number. The shock locations differ between the wind-tunnel and flight data at $\eta = 0.40, 0.59$, and 0.76. However, the absolute C_p levels over the supercritical flattop profiles at the four semispan stations agree well. The following section will discuss the sensitivity of the upper-surface C_p distributions at $\eta = 0.76$ to small Mach number changes near the design cruise condition of $M_\infty = 0.85$.

Mach Number Effects

Figure 7 compares the upper- and lower-surface C_p distributions at $\eta = 0.76, \alpha = 8°$ and $\delta_{LE/TE} = 0/2$ for large and small changes in Mach number. Figure 7(a) illustrates the development and rearward movement of the expected shock in the upper-surface C_p distributions with increasing Mach numbers ($M_\infty = 0.60, 0.80, 0.85,$ to 0.90). For $M_\infty = 0.85$, the flattop supercritical pressure profile has developed, which is similar to those shown in Fig. 6(b). The lower-surface C_p distributions show small changes with increasing Mach number. Figure 7(b) compares the C_p distributions for small changes in Mach number. This serves to illustrate the sensitivity of the C_p distributions to Mach number near the design cruise condition. The four sets of data are all from the same flight test maneuver, during which the target Mach number was 0.85. The actual flight condition varied from $M_\infty = 0.844, 0.852, 0.855$ to 0.861. Over the forward region of the flattop supercritical profiles, the four sets of flight data agree well. This agreement indicates the respective angles of attack have been matched to almost identical values (Ref. 17). The different shock locations in the upper-surface C_p distributions, however, consistently move rearward with each small M_∞ increase. As expected, the separation between the shock locations is relatively proportional to the difference between the M_∞ values. Note that this sensitivity can be shown for differences in M_∞ as small as 0.003, which is near the limits of instrumentation accuracies.

Angle-of-Attack Effects

Steady chordwise pressure distributions at $\eta = 0.76$, $M_\infty = 0.85$ and $\delta_{LE/TE} = 0/2$ are shown in Fig. 8 for four angles of attack ($\alpha = 5°, 6°, 8°$ and $12°$). This illustrates the expected rearward movement of the shock location over the supercritical airfoil as α increases to $8°$. As α increases to $12°$, the flow over the aft portion of the wing chord has separated (Ref. 17).

Section normal-force coefficients c_n were obtained by integrating the measured steady pressure distributions over the four semispan stations. Selected c_n values are shown in Fig. 9 for a range of α values at $M_\infty = 0.85$ and $\delta_{LE/TE} = 0/2$. Second-order curve fits to the flight data are included to highlight the respective trends. The results from both wind-tunnel and flight tests show good agreement. The expected trend of decreasing load from the inboard to outboard semispan stations is clearly shown at each α.

Camber Effects

Figure 10 illustrates the effects of variable-camber deflections in the steady chordwise pressure distributions at $\eta = 0.76$ for $M_\infty = 0.85$. Figure 10(a) shows the C_p distributions for three different leading-edge surface deflections of $\delta_{LE/TE} = 0/2, 5/2,$ and $10/2$. Although there are some changes in the aft shock locations of the three upper-surface C_p distributions, the most significant changes occur in both the upper and lower C_p distributions near the leading edge. As expected, with increasing leading-edge camber deflection the location for $C_p = 0$ moves. This is shown by the leading-edge suction peak on the upper surface going from a negative C_p value at $\delta_{LE/TE} = 0/2$, to a positive value at $\delta_{LE/TE} = 10/2$. The corresponding lower-surface C_p distributions near the leading edge indicate an opposite change. Thus the location for $C_p = 0$ has moved from near $x/c = 0.0$ at $\delta_{LE/TE} = 0/2$, to $x/c = 0.1$ on the lower surface at $\delta_{LE/TE} = 10/2$.

Figure 10(b) shows the C_p distributions for three different trailing-edge surface deflections of $\delta_{LE/TE} = 5/2, 5/6,$ and $5/10$. The leading-edge region of the C_p distributions are nominally unaffected, but as expected, the trailing-edge C_p distributions indicate the increasing load, or c_n, with increasing trailing-edge camber deflection. The upper-surface C_p distribution at $\delta_{LE/TE} = 5/10$ also indicates possible separated flow near the trailing edge.

Figure 10(c) shows the C_p distributions for three different angles of attack at $\delta_{LE/TE} = 5/6$. For $\alpha = 5°$, the upper-surface C_p distribution downstream from the shock location (near $x/c = 0.4$) has a secondary region of negative pressure rise, which then recovers near the trailing edge. As α increases to $8°$, the

shock location moves aft along the upper surface and the leading-edge suction peak level increases. At $\alpha = 11°$, the upper surface C_p distribution level along the forward half of the wing chord has further increased. However, at this high α condition the upper-surface C_p distribution aft of midchord does not have a strong shock region because the flow has separated at the trailing edge.

Figures 11(a) and (b) show c_n values over a range of α for three different leading- and trailing-edge camber deflections, respectively, at $M_\infty = 0.85$. Second-order curve fits to the flight data are also included. The c_n values are derived from flight data over the wing chord at $\eta = 0.76$ such as the C_p distributions shown in Figs. 10(a), (b), and (c). Figure 11(a) compares the c_n characteristics for the three leading-edge surface deflections of $\delta_{LE/TE} = 0/2$, $5/2$, and $10/2$. Curves for the data at $\delta_{LE/TE} = 0/2$ and $\delta_{LE/TE} = 5/2$ are almost identical. The $\delta_{LE/TE} = 10/2$ data curve is also similar for α values below 8°. The c_n levels for $\alpha > 8°$ at $\delta_{LE/TE} = 10/2$, are lower than those at $\delta_{LE/TE} = 0/2$ and $\delta_{LE/TE} = 5/2$. Figure 11(b) compares the c_n characteristics for the three trailing-edge surface deflections of $\delta_{LE/TE} = 5/2$, $5/6$, and $5/10$. As expected for a given α, c_n increases with increasing trailing-edge surface deflection. Figure 11(c) shows the benefits to be gained by judicious selection of both leading- and trailing-edge camber deflections. The variable camber curve is constructed from the optimum c_n values at each α for selected data in Figs. 11(a) and (b). The design cruise camber curve is shown for reference. The higher c_n distribution with increasing α shown for the variable-camber curve in Fig. 11(c) is similar to the trend for conventional high-lift devices, as shown in Fig. 3.39 of Ref. 19. A comparison of the effects of variable-camber drag with the AFTI/F-111 cruise wing and TACT wing can be found in Ref. 9.

Comparison of TACT and MAW Flight Data

To compare with TACT flight data, MAW flight data were taken at several Mach numbers, angles of attack, and dynamic pressures (Refs. 2, 20). Only the design cruise camber shape (MAW at $\delta_{LE/TE} = 0/2$) of the respective wings at $\Lambda_{LE} = 26°$ is considered. Typical comparisons for the MAW and TACT C_p data at $M_\infty = 0.70$ and 0.85, $q_\infty = 300$ lb/ft^2 and $R_n = 2.3 \times 10^6$ ft^{-1} are shown in Figs. 12 and 13.

Figure 12 shows both TACT and MAW flight data at $M_\infty = 0.70$ for $\alpha = 6°$ and 8°. In Fig. 12(a) the

data compare well except for the leading-edge suction peak and over the aft section ($0.75 < x/c < 0.95$) of the upper surface. The C_p data over this aft section of the MAW indicates that design changes from the original TACT wing (Ref. 10) to reduce the secondary negative pressure rise were successful. In Fig. 12(b) the C_p distributions match well at $\alpha = 8°$ except for the same aft section discussed earlier. In general, the levels of C_p data match well over much of the upper surface and all the lower surface at $M_\infty = 0.70$.

Figure 13 compares TACT and MAW steady chordwise pressure data at the design cruise Mach number of 0.85. For $\alpha = 6°$ in Fig. 13(a), the C_p distributions match well except at the shock location and at the aft section of the upper surface. Since the TACT wing was modified for the MAW design to reduce the secondary negative pressure rise over this aft section, some changes in the shock locations and the shape of the C_p pressure profiles are to be expected. With increasing α the differences between the TACT and MAW shock locations diminish until good agreement exists at $\alpha = 8°$, as shown in Fig. 13(b). Additional comparisons of TACT and MAW data should add to the understanding of the pressure fields over both wings.

Comparison of Predicted and MAW Flight Data

With the increasing reliance on computational aerodynamics for many of today's developmental studies (Refs. 21, 22), evaluation of such capabilities with flight test data helps define limitations and areas for improvement. The quality of aerodynamic predictions is directly determined by how well a particular phenomenon has been defined and modeled. The proper interpretation of predicted aerodynamics provides the aerodynamicist with relative trends and features of the flow field, not necessarily exact estimates of absolute performance values such as drag (Ref. 23). The use of computational fluid dynamics (CFD) methods as analytical tools or design tools demands very careful application and interpretation of the results.

This section will present results from a computational method that is representative of the various types used during the MAW airfoil and wing design process (Refs. 7, 10). Comparisons between measured and calculated steady pressure distributions will be at the design cruise Mach number of 0.85. As noted previously, the computational model is based on the measured geometric shape of a 1/12-scale wind-tunnel

6

model for the design cruise conditions of $\delta_{LE/TE}$ = 0/2 and Λ_{LE} = 26°. An established production class CFD code was chosen to provide preliminary predictions of the surface pressure distributions on the MAW. The transonic airfoil analysis (TAA) method is a local version of the Bauer, Garabedian, Korn, and Jameson program (Ref. 24). This method is a two-dimensional formulation of the nonconservative solution to the full potential flow equation, with viscous effects simulated by boundary-layer displacement additions to the airfoil surface. The boundary-layer displacement is calculated using a Nash-MacDonald integral boundary-layer procedure (Ref. 25) that is iteratively updated during the potential solution convergence. The Mach numbers input to the TAA code ($M_\infty \cos \Lambda_{LE}$) were adjusted by simple sweep theory (Ref. 18). Although the applicability of simple sweep theory is compromised at supercritical conditions due to strong shocks or possible flow separation on the wing, it does provide direct comparison between the two-dimensional calculations and three-dimensional flight test results. A three-dimensional version of the TAA code known as FLO22.NM (Refs. 26, 27, 28, 29) has been selected to provide a more comprehensive aerodynamic analysis of the MAW, however, results are unavailable at this time.

The TAA code was run at subcritical conditions (that is, at subsonic speed and α combinations below that for strong shock or separated flow development) such as that shown for the experimental data in Fig. 6(a). The TAA code solution process can be initiated by either prescribing an α value or a section normal-force coefficient value c_n. The C_p distributions over the four wing chord locations of the MAW ($\eta = 0.40, 0.59, 0.76$ and 0.93.) were solved by the TAA code for given α values. As expected, the comparisons between flight data and predictions for M_∞ = 0.60, which are not shown, were very good. By using c_n values equal to those derived from flight data, another set of calculated C_p distributions were produced. The comparisons between these predictions and flight data were better, especially for the absolute leading-edge suction peak levels. However, solving for C_p distributions based on a known c_n value were not made in order to improve comparisons. The purpose was to provide predicted C_p distributions based on either prescribing an α value or c_n. The two applications are synonymous with using the code as an analytical tool or for design considerations. At subcritical conditions the resultant C_p distributions for the MAW were almost identical for either application. The next section will discuss

the limitations of applying the code near supercritical conditions.

Defining the limitations of a specific CFD code over a range of flow conditions such as M_∞ and α for a given geometric configuration is often called "calibrating" the code. Just as an airplane has a flight envelope, a CFD code has a similar convergence envelope based on theoretical assumptions such as fully attached flow. Figure 14 shows the range of convergence for the TAA computational models for two envelopes at η = 0.40 and η = 0.93. Nonconvergence of the code can be simply defined as the limit of M_∞ and α combinations that exceed attached flow conditions. As expected, the usable α range for the code decreases with increasing M_∞. The difference between the two envelopes also indicates the effect of spanwise geometric changes such as relative twist and thickness between the two airfoils. The following section will present TAA code calculations at η = 0.76 and M_∞ = 0.85 for three different camber deflection models. The calculations are near the convergence envelope boundary of the code.

At the cruise condition of the MAW (M_∞ = 0.85, $\delta_{LE/TE}$ = 0/2 and Λ_{LE} = 26°) a family of curves were generated for calculated C_p distributions at η = 0.76 over a prescribed range of α values. Figure 15 illustrates a typical result of the data comparison for upper-surface C_p distributions over the airfoil at η = 0.76. The c_n values listed in Fig. 15 are based on the integration of the respective C_p distributions. In general the trend of the flight data at α = 6° is similar to the predicted data at α = 8°, but the respective c_n values are considerably different. The development of the typical flattop profile in the upper-surface C_p distribution as a function of changing α is clearly illustrated by the calculated C_p distributions. The usefulness of showing the predictions over a range of α values, although qualitative, is sufficient for preliminary evaluation of the flight data.

Figures 16(a) and (b) show typical comparisons of predicted and flight data for two off-design camber deflections at η = 0.76. The calculated results were arbitrarily chosen from family-of-curve-type comparisons, such as Fig. 15. Only the predictions that were representative of the trends in the flight data are shown. The chordwise C_p distributions shown in Fig. 16(a) are for a camber deflection of $\delta_{LE/TE}$ = 10/2. Note the difference between the corresponding α and c_n values for the calculated and flight data. An empirical adjustment of the predicted chordwise C_p distribution based on matching either the α or c_n values to

7

flight data would not improve this comparison. But again, the comparison is sufficient to provide insight into the flow characteristics of an off-design condition where there was only limited wind-tunnel data prior to flight. Figure 16(b) shows the chordwise C_p distributions for a camber deflection of $\delta_{LE/TE} = 5/6$. This particular camber deflection is representative of an off-design condition not specifically studied (no available wind-tunnel data) prior to flight. However, the computational model was easily generated and an extensive analysis for $\delta_{LE/TE} = 5/6$ was accomplished. The resultant comparison, especially over the upper surface of the trailing-edge camber deflection, quickly defined areas that require more detailed analysis. The predicted trend of the upper-surface C_p distribution in this region obviously exceeds the corresponding flight data. However, the number of measured data points over this trailing-edge region must also be considered when comparing them with predicted data.

Concluding Remarks

Selected results from the AFTI/F-111 MAW flight test database are presented in the form of chordwise distributions of pressure coefficients C_p and section normal-force coefficients c_n. This set of flight data includes design cruise ($\delta_{LE/TE} = 0/2$ and $\Lambda_{LE} = 26°$) and off-design wing camber deflections at subsonic Mach numbers up to 0.90 and an angle-of-attack range between 5° to 12°. The influence on the data due to span effects, Mach number effects, angle-of-attack effects, and camber effects are discussed. Certain expected characteristics in the flow field about the MAW, a smooth variable-camber, advanced supercritical wing are also discussed. Comparisons are made between the MAW flight data and corresponding MAW wind-tunnel data, TACT flight data, and predicted data.

Both the MAW flight and wind-tunnel-measured chordwise pressure distributions at four semispan locations are very similar for $M_\infty = 0.60$. The expected development of the flattop profile, typical of upper-surface C_p distributions on supercritical airfoils near the MAW design cruise condition of $M_\infty = 0.85$, is clearly shown. The shock locations of flight and wind-tunnel data near $M_\infty = 0.85$ are different.

Typical characteristics of chordwise C_p distributions on the MAW for changes in Mach number, angle of attack, and wing camber deflection are shown at $\eta = 0.76$. The movement of the shock location on the upper surface of the wing chord is shown for both large

and small changes in Mach number. These shock locations are shown to be very sensitive to small changes in Mach number near $M_\infty = 0.85$. The development of features in the pressure field such as the leading-edge suction peak and trailing-edge separation are shown for changes in angle of attack and wing camber deflections. As expected, certain off-design camber deflections over a range of α values produce an increase in the associated c_n values, as compared to those for the design cruise camber at $M_\infty = 0.85$.

Some comparisons of the TACT and MAW flight data are shown for the chordwise C_p distributions at $\eta = 0.76$. Only two Mach number and two angle-of-attack conditions are considered. Since the TACT wing was modified for the MAW design to reduce a secondary negative pressure rise near the trailing edge, some expected changes in the shock locations and the shape of the C_p pressure profiles are shown.

As expected the computational predictions of the MAW steady chordwise pressure distributions agreed well at subcritical flight conditions (M_∞ and α combinations below that for strong shock or separated flow development). The predictions at the design cruise condition ($M_\infty = 0.85$, $\delta_{LE/TE} = 0/2$ and $\Lambda_{LE} = 26°$), and most of the critical off-design flight conditions, were sufficient for preliminary qualitative analysis. This helped to define areas where more detailed analysis should be made.

Acknowledgment

References

[1] Painter. W.D. and Caw, L.J., "Design and Physical Characteristics of the Transonic Aircraft Technology (TACT) Research Aircraft," NASA TM 56048, 1979.

[2] "Symposium on Transonic Aircraft Technology (TACT)," AFFDL-TR-78-100, August 1978.

[3] "Supercritical Wing Technology: A Progress Report on Flight Evaluations," NASA SP 301, 1972.

[4] Bonnema, K.L. and Smith, S.B., "AFTI/F-111 Mission Adaptive Wing Flight Research Program," AIAA 88-2118, May 1988.

[5] Savacool, J.S. and Householder, N.F., "AFTI/F-111 Mission Adaptive Wing Wind Tunnel Pressure Report, NASA Ames Research Center, 11T Test No. 314-

1-11," Volumes 1 and 2, Boeing Document No. D365-10045-2, 1980.

[6] Wright, L.L. and Nelson, D.W., "AFTI/F-111 Mission Adaptive Wing Wind Tunnel Data Report: Arnold Engineering Development Center, PWT-16T, Test No. TF 550," Boeing Document No. D365-10024-1, 1980.

[7] Gould, D.K., "Boeing Pre-Design of AFTI-111 Mission Adaptive Wing, Volume II - Aerodynamic Trade Studies, Theoretical Calculations and Wind Tunnel Tests," AFFDL- TR-78-73, 1978.

[8] Thomasson, R., "Software Requirements Specification For AFTI/F-111 MAW Automatic Flight Control System," Boeing Document No. D365-10086-1, Revision L, March 1987.

[9] Smith, S.B. and Nelson, D.W., "Determination of the Aerodynamic Characteristics of the Mission Adaptive Wing," AIAA 88-2556, June 1988.

[10] Nelson, D.W., "AFTI/F-111 Aerodynamics Final Report," Boeing Document No. D365-10110-1, February 1987.

[11] Wong, K.J., "AFTI/F-111 Mission Adaptive Wing Lift and Drag Flight Test Results," Vol. I, AFFTC TR-87-02, April 1987.

[12] Curley, M.A. and Rufsvold, K., Maj., USAF, "AFTI/F-111 Mission Adaptive Wing Stability and Control," AFFTC TR-87-01, June 18,1987.

[13] Fehl, J.E., "AFTI/F-111 Mission Adaptive Wing 1/12 Scale Wind Tunnel Model Inspection," AFWAL-TM-80-114-FIMS, December 1980.

[14] Bussing, P.R., "AFTI F-111 Final Instrumentation Report," Boeing Document No. D365-10016-2, 1984.

[15] Webb, L.D. and Washington, H.P., "Flight Calibration of Compensated and Uncompensated Pitot-Static Airspeed Probes and Aplication of the Probes to Supersonic Cruise Vehicles," NASA TN D-6827, 1972.

[16] Sakamoto, G.M., "Aerodynamic Characteristics of a Vane Flow Angularity Sensor System Capable of Measuring Flightpath Accelerations for the Mach Number Range From 0.40 to 2.54," NASA TN D-8242, 1976.

[17] Montoya, L.C. and Banner, R.D., "F-8 Supercritical Wing Flight Pressure, Boundary-Layer, and Wake Measurements and Comparisons With Wind Tunnel Data," NASA TM X-3544, 1977.

[18] Moulden, T.H., "Fundamentals of Transonic Flow," John Wiley & Sons, Inc., N.Y., 1984.

[19] McCormick, B.W., "Aerodynamics, Aeronautics, and Flight Mechanics," John Wiley & Sons, Inc., N.Y., 1979.

[20] Kinsey, D.W., "Wind Tunnel/Flight Test Comparison of Wing Surface Static Pressures on the F-111/TACT (Transonic Aircraft Technology) Configuration," AFWAL-TR-84-3021, July 1984.

[21] Nixon, D., ed., "Transonic Aerodynamics," Volume 81 Progress In Astronautics and Aeronautics, 1982, American Institute of Aeronautics and Astronautics, Inc.

[22] Jameson, A., "Successes and Challenges in Computational Aerodynamics," AIAA 87-1184, June 1987.

[23] Ballhaus, W.F., Jr., "Computational Aerodynamics and Design," NASA TM 84257, 1982.

[24] Bauer, F., Garabedian, P., Korn, D., and Jameson, A., "Supercritical Wing Sections II," Lecture Notes in Economics and Mathematical Systems, Vol. 108, Springer-Verlag, New York, 1975.

[25] Nash, J.F. and Macdonald, A.G.J., "The Calculation of Momentum Thickness in a Turbulent Boundary Layer at Mach Numbers Up to Unity," ARC CP No. 963, 1967.

[26] Jameson, A. and Caughey, D.A., "Numerical Calculation of the Transonic Flow Past a Swept Wing," C00-3077-140, ERDA Math. and Comput. Lab., New York Univ., June 1977 (also available as NASA CR-153297).

[27] Hicks, R.M. and Henne, P.A., "Wing Design by Numerical Optimization," AIAA 77-1247, August 1977.

[28] Henne, P.A., and Hicks, R.M., "Wing Analysis Using a Transonic Potential Flow Computational Method," NASA TM-78464, 1978.

[29] Newman, P.A., Carter, J.E., and Davis, R.M., "Interaction of a Two-Dimensional Strip Boundary Layer With a Three-Dimensional Transonic Swept Wing Code," NASA TM-78640, 1978.
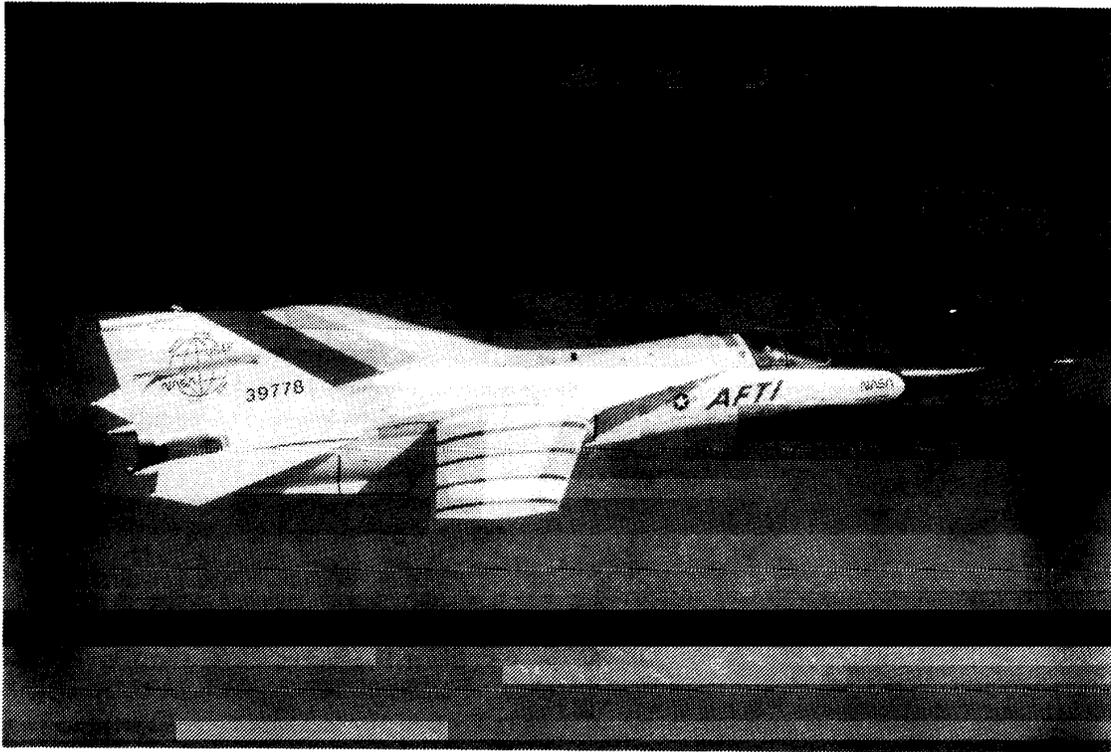
EC85 33205 017

Fig. 1 In-flight photograph of AFTI/F-111 MAW. Chordwise dark lines on the right wing indicate the four semispan locations of pressure orifices.
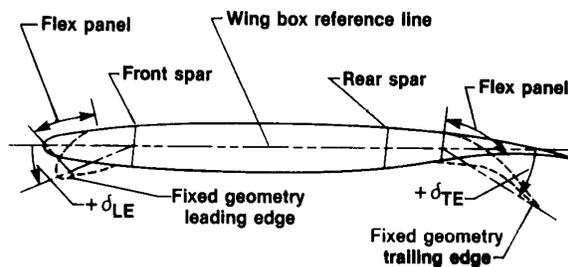

*Fig. 2 Photograph and sketch of the MAW smooth, variable-camber flap shape.*

10

Fig. 4 Sketch of semispan locations of surface pressure orifices and static pressure instrumentation for the right wing of the AFTI/F-111 MAW.
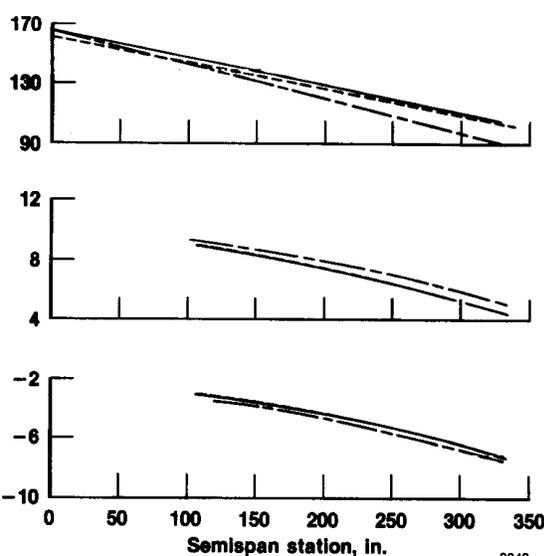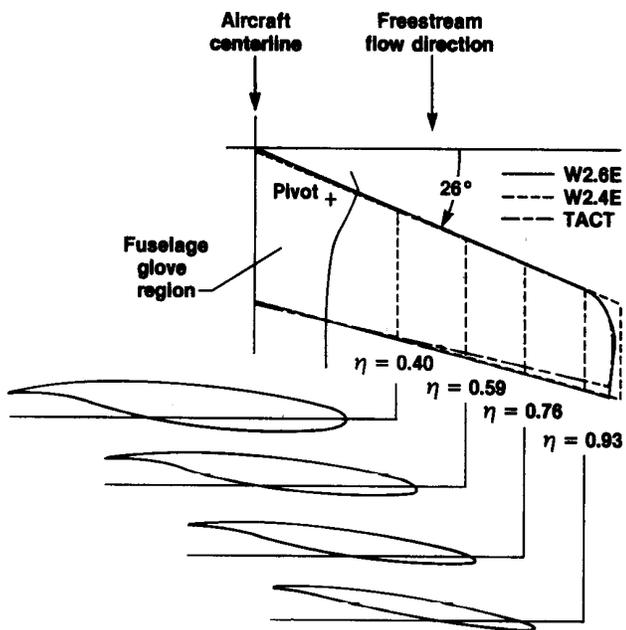
Fig. 3 Comparison of wing geometric characteristics.
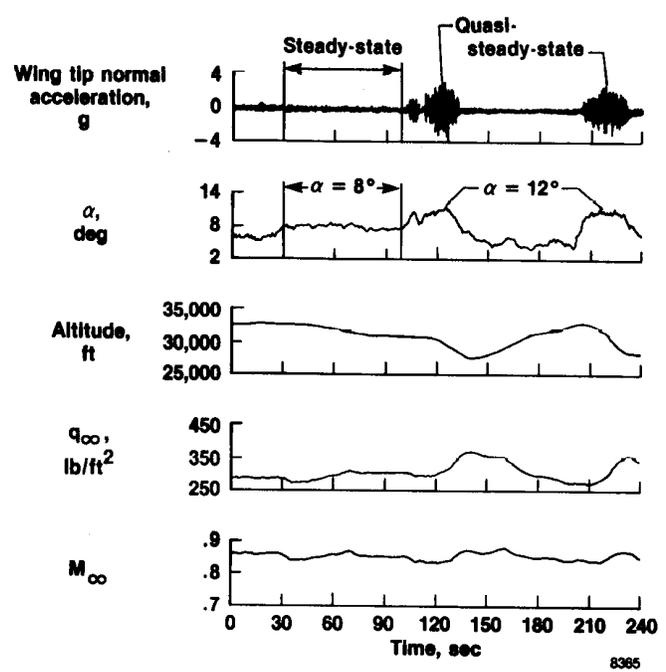
Fig. 5 Time history of flight parameters during a typical maneuver to obtain steady pressure measurements.

11
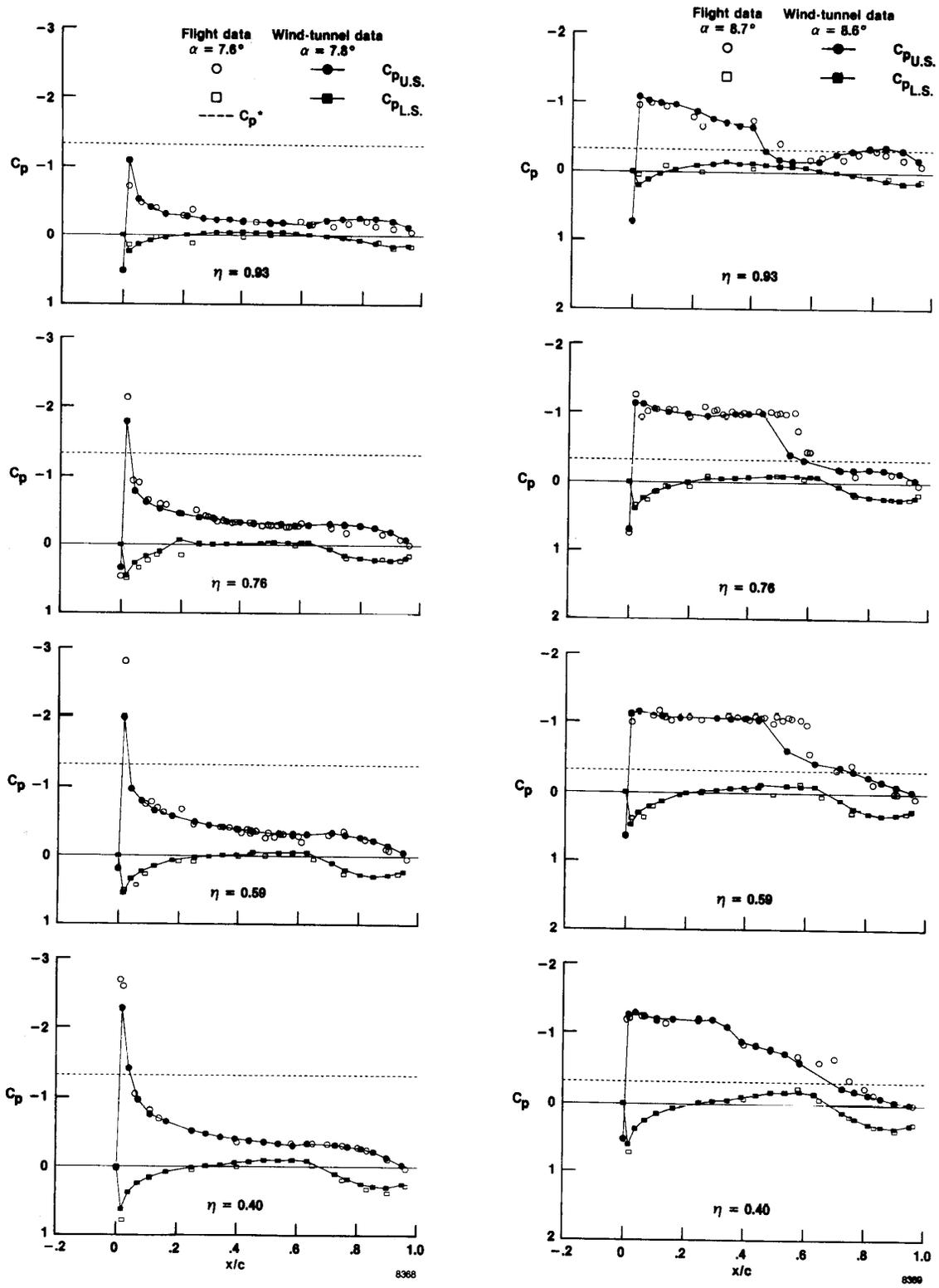
(a) $M_\infty = 0.60$.

(b) $M_\infty = 0.85$.

Fig. 6 Steady chordwise pressure distributions at four semispan stations for $\delta_{LE/TE} = 0/2$.

Flight data

○ $M_\infty = 0.608$
□ $M_\infty = 0.797$
◇ $M_\infty = 0.852$
△ $M_\infty = 0.901$

$C_{P_{U.S.}}$ = Open symbols

$C_{P_{L.S.}}$ = Solid symbols

8350

(a) Large Mach number range.

Flight data

○ $M_\infty = 0.844$
□ $M_\infty = 0.852$
◇ $M_\infty = 0.855$
△ $M_\infty = 0.861$

8351
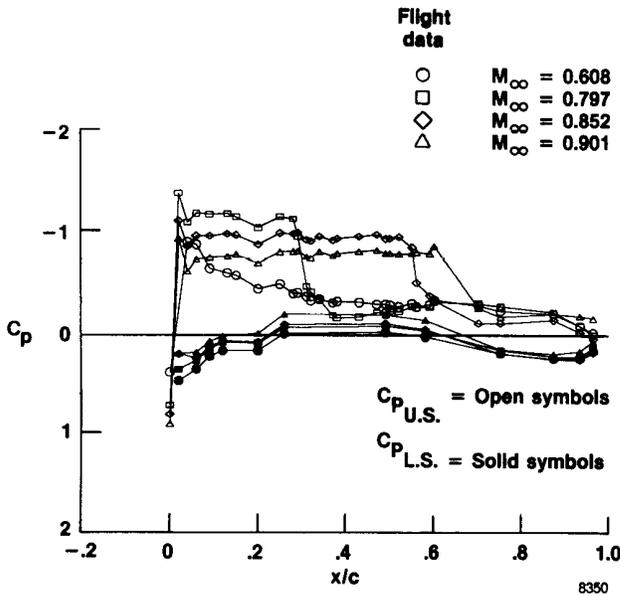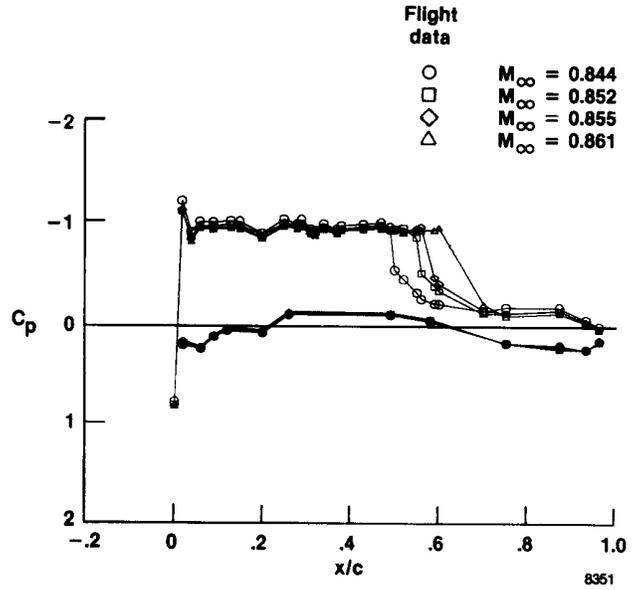
(b) Small Mach number range.

Fig. 7 Steady chordwise pressure distributions for both large and small ranges of Mach number; $\eta = 0.76$, $\delta_{LE/TE} = 0/2$.


Flight data

○ $\alpha = 5°$
□ $\alpha = 6°$
◇ $\alpha = 8°$
△ $\alpha = 12°$

$C_{P_{U.S.}}$ = Open symbols

$C_{P_{L.S.}}$ = Solid symbols

8352
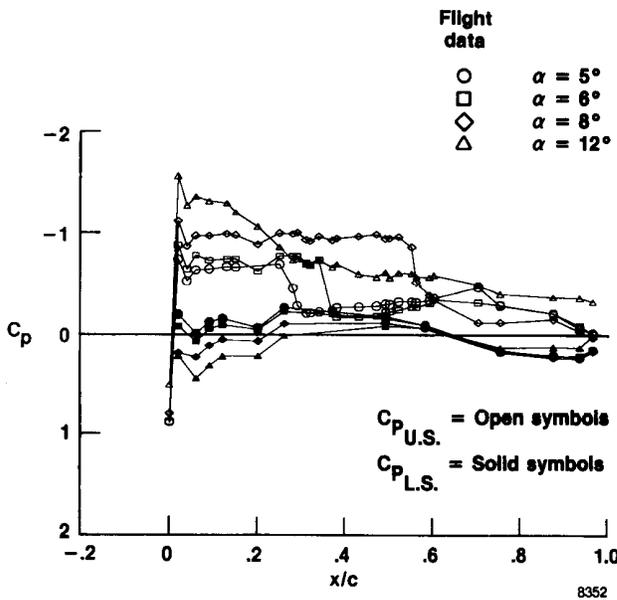
*Fig. 8 Steady chordwise pressure distributions for four angles of attack at* $\eta = 0.76$; $M_\infty = 0.85$, $\delta_{LE/TE} = 0/2$.

Flight data   2nd order curve fit

○ ———— $\eta = 0.40$
□ ············ $\eta = 0.59$
◇ —·—·— $\eta = 0.76$
△ ———— $\eta = 0.93$

Wind-tunnel data = Solid symbols

8353
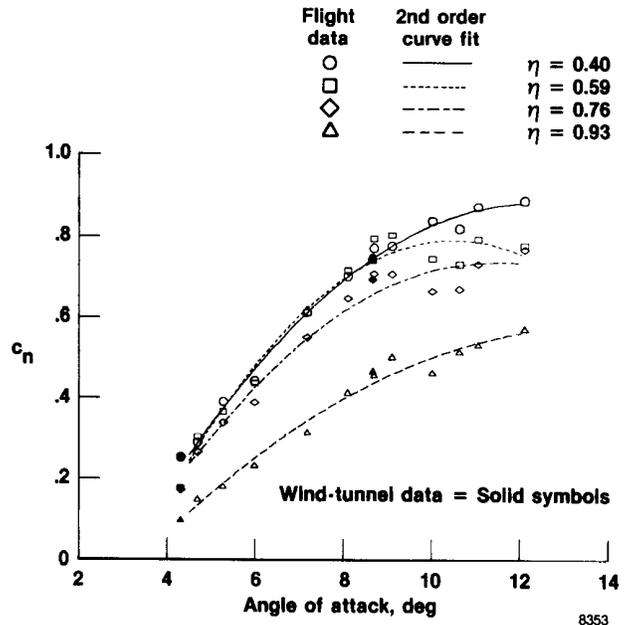
Fig. 9 Section normal-force coefficients as a function of α *at four semispan stations;* $M_\infty = 0.85$, $\delta_{LE/TE} = 0/2$.
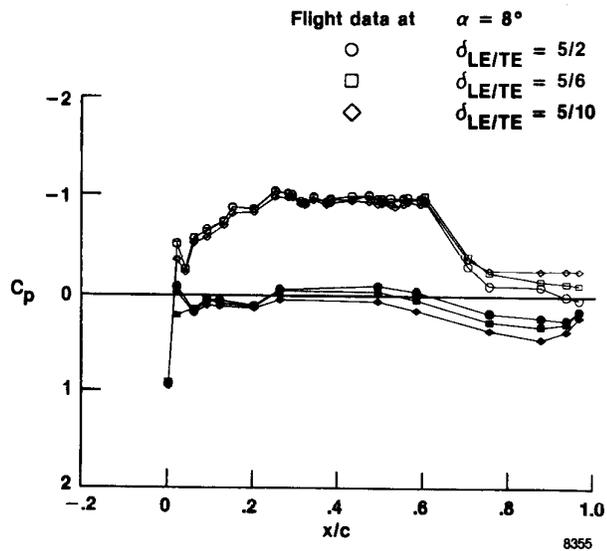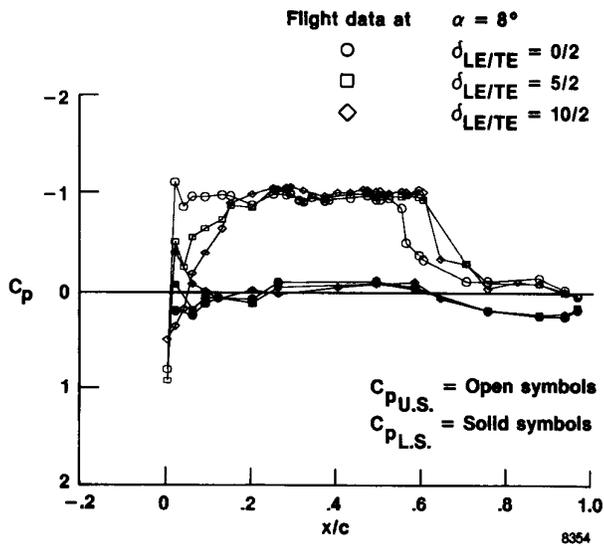
13

(a) Three different leading-edge surface deflections.

(b) Three different trailing-edge surface deflections.
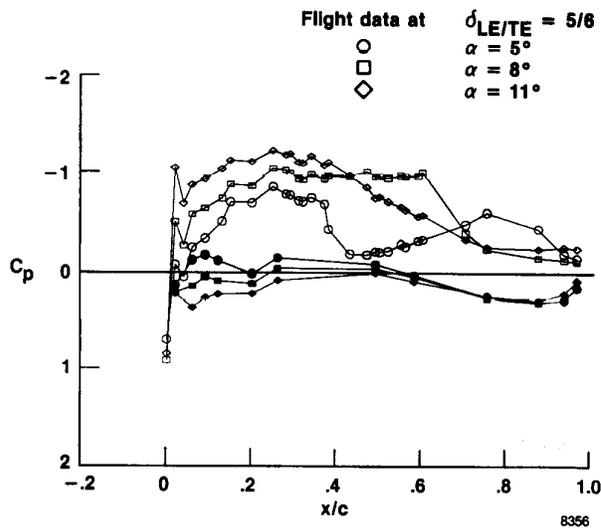
(c) Three different angles of attack.

Fig 10. Steady chordwise pressure distributions for various camber deflections at $\eta = 0.76$ and $M_\infty = 0.85$.
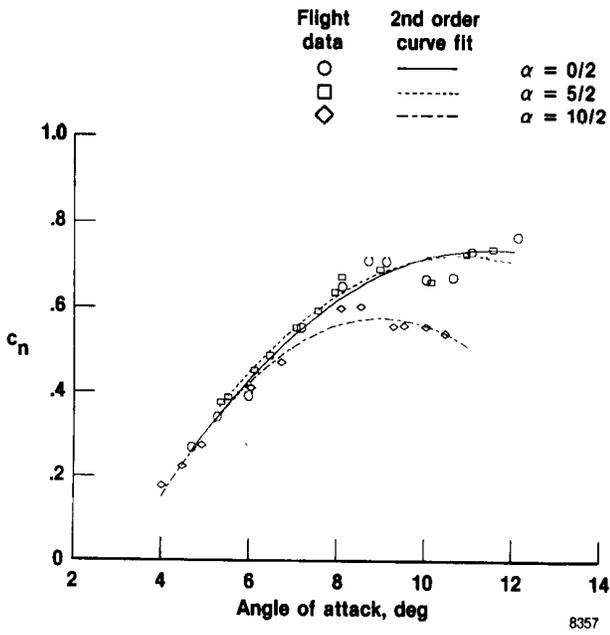
14

(a) Three different leading-edge surface deflections.

(b) Three different trailing-edge surface deflections.

Flight data

O $\delta_{LE/TE} = 0/2$
□ $\delta_{LE/TE} = 5/2$
◇ $\delta_{LE/TE} = 5/6$
△ $\delta_{LE/TE} = 5/10$
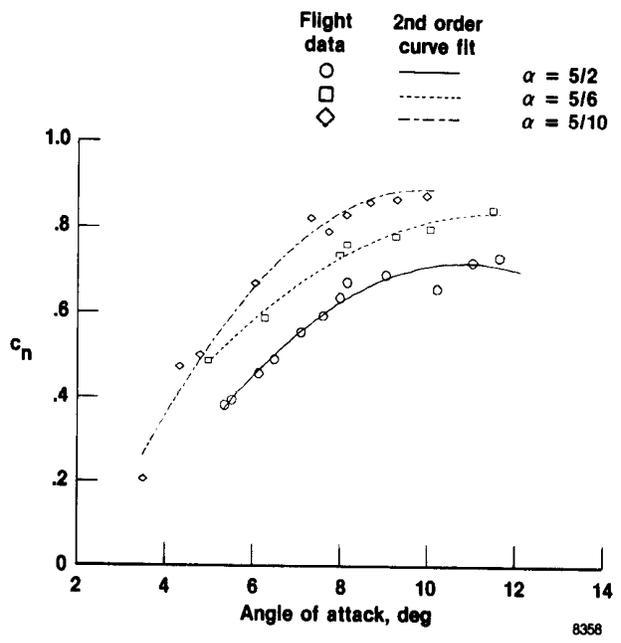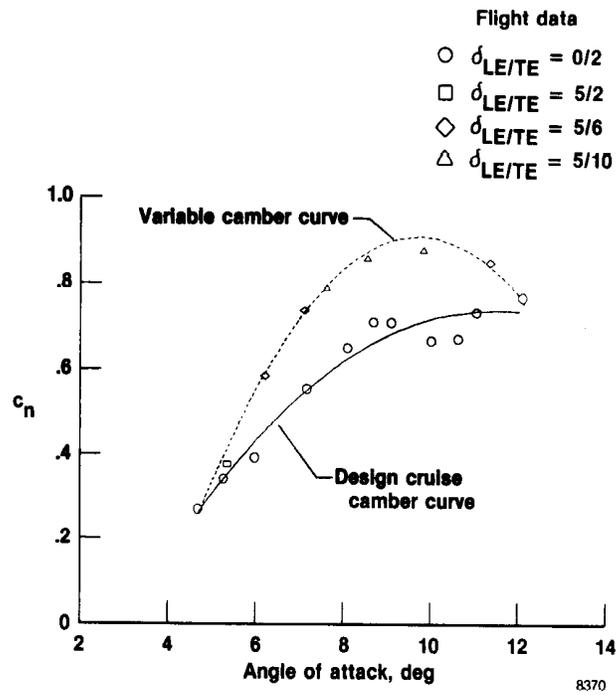
(c) Camber combinations for optimum c_n as a function of α.

Fig. 11 Section normal-force coefficients as a function of α for various camber deflections at $\eta = 0.76$ and $M_\infty = 0.85$.

15

(a) $\alpha = 6°$.

(b) $\alpha = 8°$.
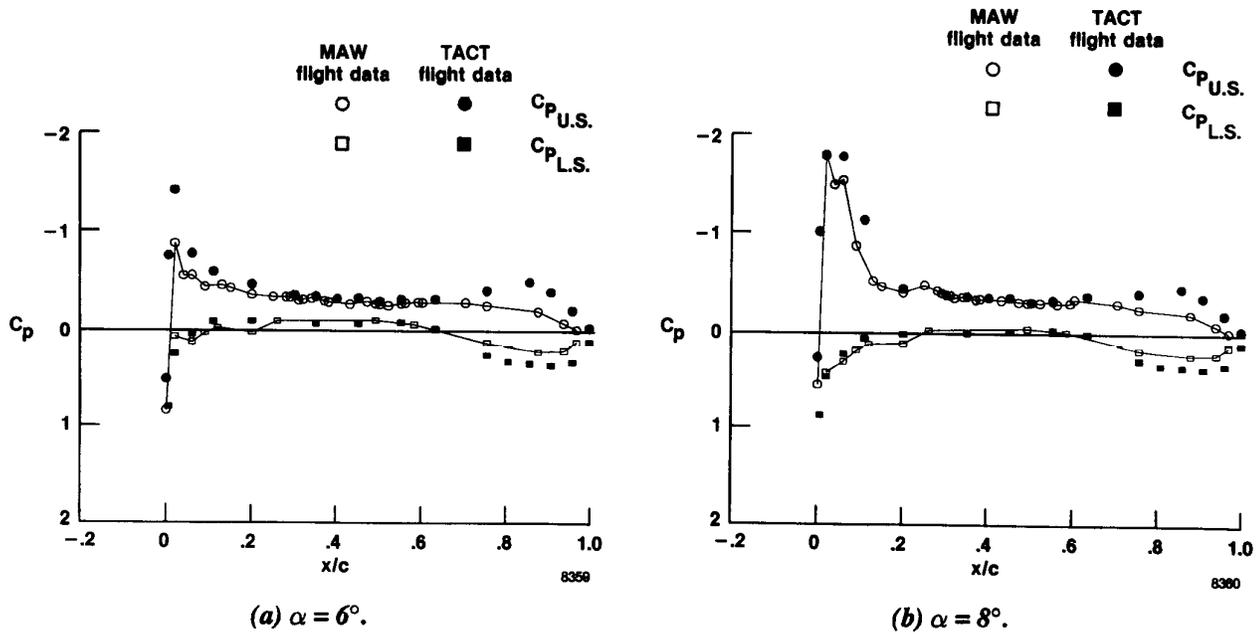
Fig. 12 Comparison of TACT and MAW steady chordwise pressure distributions for two angles of attack at $\eta = 0.76$; $M_\infty = 0.70$, $\delta_{LE/TE} = 0/2$.


(a) $\alpha = 6°$.

(b) $\alpha = 8°$.
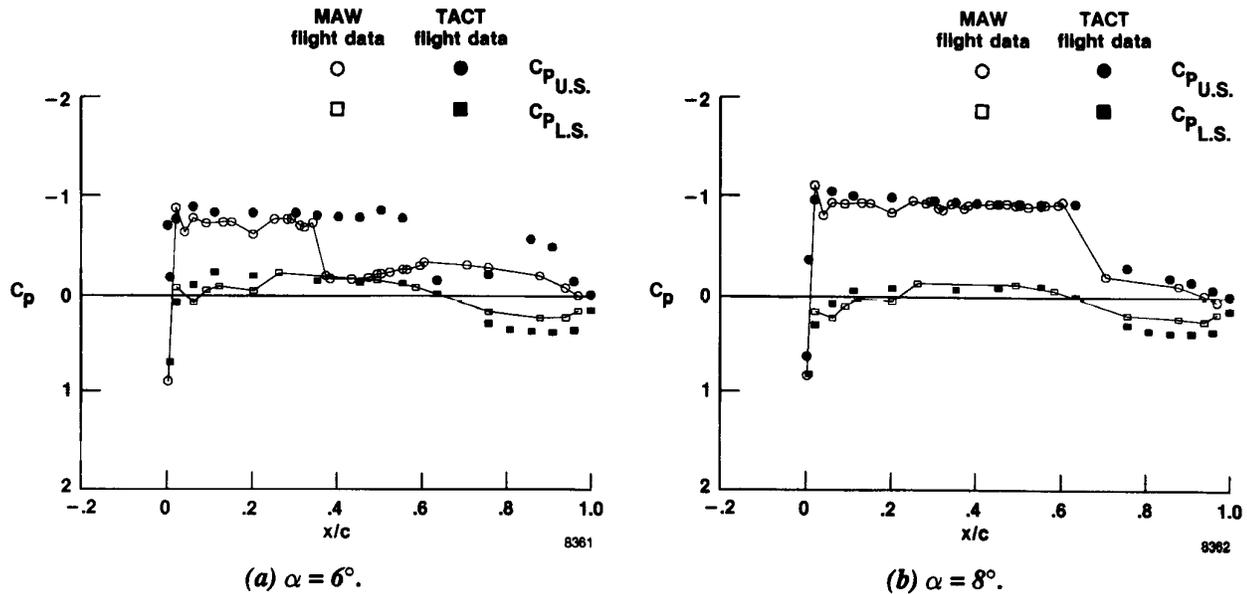
Fig. 13 Comparison of TACT and MAW steady chordwise pressure distributions for two angles of attack at $\eta = 0.76$; $M_\infty = 0.86$, $\delta_{LE/TE} = 0/2$.

16

$(M_\infty \cos \Lambda_{LE})$

M_∞

α, deg

8363
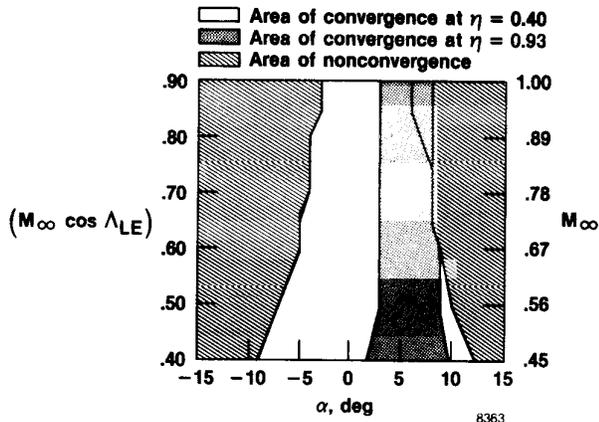
Fig. 14 TAA code convergence envelopes for two airfoil sections of the MAW at $\delta_{LE/TE} = 0/2$ and $\Lambda_{LE} = 26°$.

$C_{p_{U.S.}}$

○   Flight data at $\alpha = 6°$, $c_n = 0.388$
——   Calculated at $\alpha = 6°$, $c_n = 0.371$
- - -   Calculated at $\alpha = 7°$, $c_n = 0.551$
— —   Calculated at $\alpha = 8°$, $c_n = 0.741$

x/c

8364
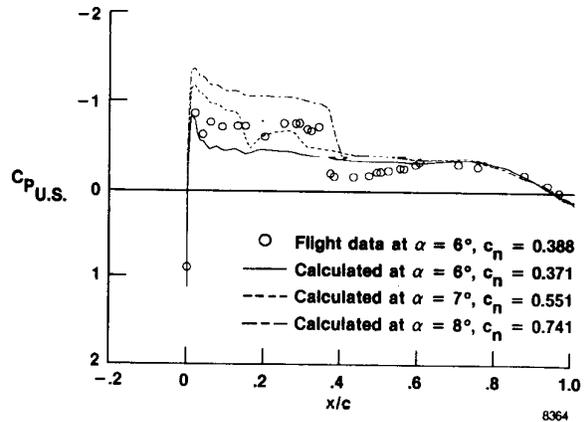
Fig. 15 Comparison of predicted and MAW upper-surface C_p distributions at $\eta = 0.76$; $M_\infty = 0.85$, $\delta_{LE/TE} = 0/2$.

Flight data at $\alpha = 4.9°$ Calculated at $\alpha = 7.0°$
$(c_n = 0.271)$ $(c_n = 0.534)$

○ —— $C_{p_{U.S.}}$
□ - - - - $C_{p_{L.S.}}$

C_p

x/c

8366

(a) $\delta_{LE/TE} = 10/2$.

Flight data at $\alpha = 4.9°$ Calculated at $\alpha = 5.0°$
$(c_n = 0.477)$ $(c_n = 0.922)$

○ —— $C_{p_{U.S.}}$
□ - - - - $C_{p_{L.S.}}$

C_p

x/c

8367
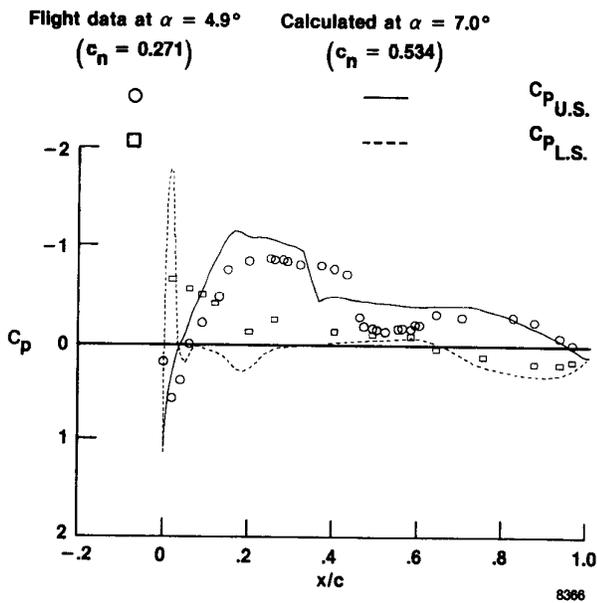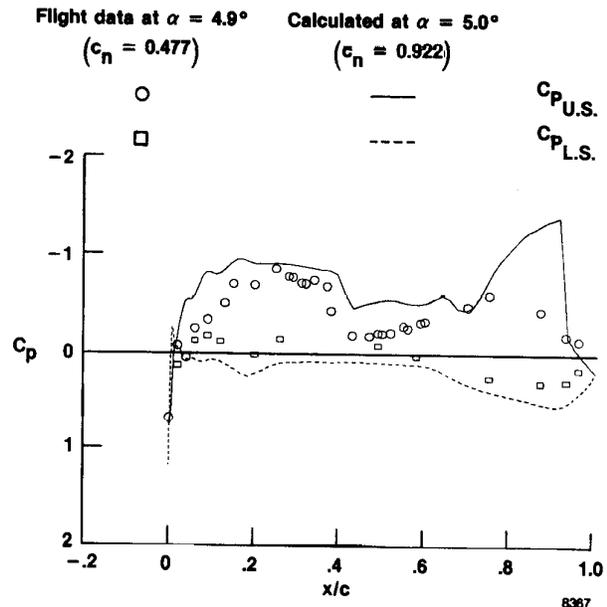
(b) $\delta_{LE/TE} = 5/6$.

Fig. 16 Comparison of predicted and MAW steady chordwise pressure distributions for two off-design camber deflections at $\eta = 0.76$; $M_\infty = 0.85$.

17

NASA
National Aeronautics and Space Administration

Report Documentation Page

1. Report No. NASA TM-100443	2. Government Accession No.	3. Recipient's Catalog No.
4. Title and Subtitle Measured and Predicted Pressure Distributions on the AFTI/F-111 Mission Adaptive Wing		5. Report Date November 1988
		6. Performing Organization Code
7. Author(s) Lannie D. Webb, William E. McCain, and Lucinda A. Rose		8. Performing Organization Report No. H-1495
		10. Work Unit No. RTOP 533-0211
9. Performing Organization Name and Address NASA Ames Research Center Dryden Flight Research Facility P.O. Box 273, Edwards, CA 93523-5000		11. Contract or Grant No.
		13. Type of Report and Period Covered Technical Memorandum
12. Sponsoring Agency Name and Address National Aeronautics and Space Administration Washington, DC 20546		14. Sponsoring Agency Code

15. Supplementary Notes

Prepared as AIAA 88-2555 for presentation at the Sixth Applied Aerodynamics Conference, Williamsburg, Virginia, June 6–8, 1988.

16. Abstract

Flight tests have been conducted using an F-111 aircraft that has been modified with a mission adaptive wing (MAW). The MAW has variable-camber leading and trailing edge surfaces that can change the wing camber in flight, while preserving smooth upper surface contours. This paper contains wing surface pressure measurements obtained during flight tests at Dryden Flight Research Facility of NASA Ames Research Center. Upper and lower surface steady pressure distributions were measured along four streamwise rows of static pressure orifices on the right wing for a leading-edge sweep angle of 26°. The airplane, wing, instrumentation, and test conditions are discussed. Steady pressure results are presented for selected wing camber deflections flown at subsonic Mach numbers up to 0.90 and an angle-of-attack range of 5° to 12°. The Reynolds number was 26 million, based on the mean aerodynamic chord. The MAW flight data are compared to MAW wind-tunnel data, transonic aircraft technology (TACT) flight data, and predicted pressure distributions. The results provide a unique database for a smooth, variable-camber, advanced supercritical wing.

17. Key Words (Suggested by Author(s)) AFTI/F-111, Mission Adaptive Wing, CFD predicted data, Pressure distributions, Section normal-force coefficients, and Smooth variable camber	18. Distribution Statement Unclassified — Unlimited Subject category 05		
19. Security Classif. (of this report) Unclassified	20. Security Classif. (of this page) Unclassified	21. No. of pages 18	22. Price A02

NASA FORM 1626 OCT 86

For sale by the National Technical Information Service, Springfield, VA 22161-2171.